Experimental and Numerical Flow Analysis of an Engine-Realistic State-of-the-Art Turbine Rear Structure

Citation for the original published paper (version of record):
Vikhorev, V., Nylander, P., Chernoray, V. et al (2022). Experimental and Numerical Flow Analysis of an Engine-Realistic State-of-the-Art Turbine Rear Structure. Journal of Engineering for Gas Turbines and Power, 144(7). http://dx.doi.org/10.1115/1.4054075

Valentin Vikhorev
Department of Mechanics and
Maritime Sciences,
Chalmers University of Technology,
Gothenburg SE-41296, Sweden
e-mail: valvik@chalmers.se

Pär Nylander
GKN Aerospace Engine Systems,
Trollhättan SE-46181, Sweden
e-mail: par.nylander@gknaerospace.com

Valery Chernoray
Department of Mechanics and
Maritime Sciences,
Chalmers University of Technology,
Gothenburg SE-41296, Sweden
e-mail: valery.chernoray@chalmers.se

Jonas Larsson
GKN Aerospace Engine Systems,
Trollhättan SE-46181, Sweden
e-mail: Jonas.Larsson@gknaerospace.com

Oskar Thulin
GKN Aerospace Engine Systems,
Trollhättan SE-46181, Sweden
e-mail: oskar.thulin@gknaerospace.com

Experimental and Numerical Flow Analysis of an Engine Realistic State-of-the-Art Turbine Rear Structure

This paper presents experimental and numerical CFD studies of the aerodynamics of a turbine rear structure (TRS). The TRS test geometry is an engine-realistic state-of-the-art design with a polygonal outer case, recessed engine mount bumps, and three different vane types: regular vanes, bump vanes in bump sectors, and thick vanes. Using three different sector types simultaneously was found to be crucial for the inlet boundary conditions. Experiments were performed in a modern rotating test facility with a low-pressure turbine (LPT) stage upstream of the TRS. A Reynolds number of 350,000 was used, representative of a TRS in a narrow-body geared turbofan engine. The TRS performance was analyzed both at on- and off-design conditions, and a thorough side-by-side comparison of CFD and experiments was performed. Static-pressure distributions, turning and outlet flow-angles, wakes and losses, and surface-flow visualizations and outlet total pressure contours are presented. The thick vane showed good aerodynamic performance, similar to the regular vane. For the bump vane, the mount bumps were found to generate additional local separations and secondary flows, resulting in extra losses. In the regions with strong secondary flows, CFD over-predicts the wakes, whereas the wakes around midspan, where secondary flows have a smaller influence, are predicted well.
[DOI: 10.1115/1.4054075]

1 Introduction

In a turbofan engine, the rear engine mounts are located in the turbine rear structure (TRS). This structure, placed downstream of the low-pressure turbine (LPT), contains the turbine outlet-guide-vanes (OGVs) and also holds the aft bearings for the low-pressure axis. Hence, the TRS is both a structural component, with strong structural loads, and an aerodynamic component that deswirls the flow from the last LPT rotor. In addition, the TRS vanes must provide the necessary lead-through area for oil and scavenge tubes for lubrication of the bearings. Designing a TRS that can handle both the large structural loads and deswirl the flow with low pressure losses at all important operating points is always a compromise. Recent trends to improve performance and reduce emissions, increased turbine temperatures, geared engines with an increased off-design range for the TRS, and more strict weight and length requirements have made the TRS design a challenge.

A new state-of-the-art engine representative TRS was designed with a polygonal outer case, recessed engine mounts (bumps), and 12 vanes. The configuration consists of six regular vanes, three thick vanes (also called tube vanes) with increased thickness, and three dedicated bump vanes (also called mount vanes) in the bump sectors. The regular vanes are designed solely for structural and aerodynamic functionality. The additional purpose of the thick vanes is to provide the space needed for oil pipes. The purpose of the engine mount recesses (bumps) and the polygonal shroud is to improve the structural properties of the TRS.

The TRS aerodynamics was experimentally investigated in a modern LPT-OGV test facility at the Chalmers University of Technology. This facility has a shrouded rotating LPT stage upstream of the TRS to provide engine realistic boundary conditions. This facility can reach engine representative Reynolds numbers, and by varying the turbine braking power one can investigate off-design conditions. It is a low-speed large-scale facility that runs at incompressible speeds. The flow in a real engine TRS is fully subsonic, inlet and outlet Mach numbers are around 0.5, with a maximum Mach number just below unity. Hence, the compressibility effects in a real TRS are straightforward to predict—there are no shocks and compressibility mainly influences the local density of the gas, which is easy to model numerically with an ideal gas law.

Numerical CFD analysis was performed to investigate the flow in detail and to compare the numerical results with the experiments. Comparisons were made of static-pressure distributions on the vanes and bumps, losses and wakes, turning and separations as well as secondary flows and surface flow visualizations. Tests were done both at the design point and typical off-design conditions. Overall, the numerical CFD predictions agree well with the experimental results. Further details are described below.

Turbine outlet guide vane flows have previously been studied by several researchers at Chalmers University. Hjärne et al. [1–5] made aero measurements of turbine OGVs and engine mount bumps in a linear cascade test rig. Hjärne et al. [6] also undertook extensive numerical CFD validations. To achieve more realistic inlet conditions and an annular engine representative OGV configuration, Rojo et al. [7] built a rotating test rig, and the same facility is used in this work. Rojo [8] also made initial measurements in a simplified circular TRS with only one type of vanes. Jonsson et al. extended these measurements to look at secondary flows [9] and heat transfer [10] in more detail. Deshpande et al. [11] and Jonsson et al. [12] also studied surface roughness and laminar-turbulent transition in this TRS. Vikhorev et al. [13] continued to experimentally investigate both thick vanes and engine mount bumps in this circular TRS. In 2019, the TRS component was replaced with a more engine representative geometry, having a polygonal shroud, three types of vanes (regular, thick, and bump) and recessed engine mount bumps. Initial measurements were published by Vikhorev and Chernoray [14]. This paper expands these results and adds numerical CFD validations.

The ITTM department at TU-Graz has performed several experimental and numerical studies of TRS aerodynamics. For

---

Manuscript received January 19, 2022; final manuscript received March 6, 2022; published online May 20, 2022. Editor: Jerzy T. Sawicki.

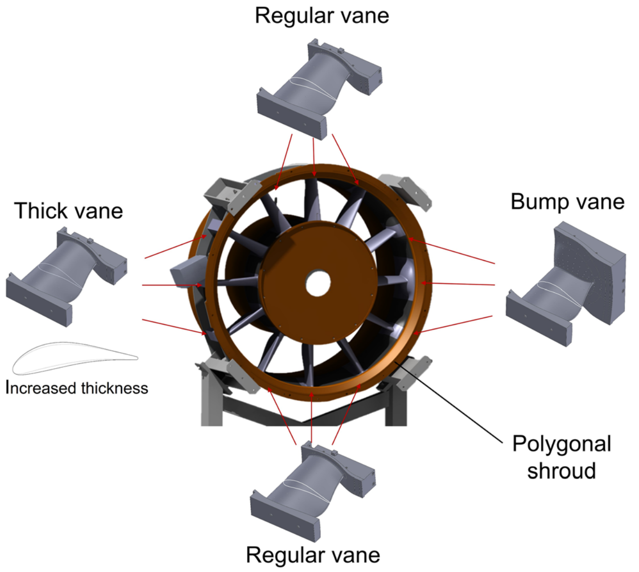

Fig. 1 Turbine rear structure with implemented outlet guide vanes

example, Selic et al. [15] studied the effect of tip leakage on the TRS, Simonassi et al. [16] studied acoustically optimized vanes and Zenz et al. [17] studied TRS vanes with riblets.

To the authors' knowledge, this work is the first publication of both experimental and numerical results for a state-of-the-art TRS with three different vane types and a three-dimensional polygonal shroud with engine mount bumps.

2 Experimental Details

In a real aero engine, the TRS at cruise has a Reynolds number, based on channel height and axial velocity, ranging from 10^5 to 6×10^5. This entire range can be covered in the test facility at the Chalmers University of Technology. Another important inlet parameter for the TRS is the inlet swirl angle and the corresponding flow coefficient (FC), defined as the ratio between the LPT's rotational speed and the axial velocity. This parameter depends on the turbine work and is controlled in Chalmers' facility by adjusting the turbine torque using a hydraulic brake.

The flow in the facility is cooled by an air–water heat exchanger in order to achieve steady temperature and flow conditions in the test section with high repeatability.

The LPT stage has 60 nozzle guide vanes (NGVs) and a shrouded turbine rotor with 72 rotor blades. Both the LPT stage and the TRS were designed by GKN specifically for this experimental rig. The designs are engine-representative, but not directly related to any real engine parts. A more detailed description of the facility design can be found in Rojo et al. [7].

A modular design of the TRS test section in the facility enables efficient customization including the possibility to modify channel geometry, any individual OGV or the entire set of OGVs. The investigated configuration of TRS was designed with a polygonal outer case, recessed engine mounts, and 12 vanes arranged as shown in Fig. 1. As shown schematically, the test section was equipped with six regular vanes, three thick vanes of increased thickness, and three bump vanes, with each bump vane having a recessed shroud bump.

Aero-measurements of the static pressure, total pressure, velocity components, and flow angles were made with two multihole probes precalibrated using in-house calibration protocols. An L-shaped five-hole probe is located upstream of the OGVs at the inlet plane and turned about 20 degrees respective to the axial direction. A straight seven-hole probe is located downstream of the OGVs at the outlet plane and positioned along the axial direction. Locations of these planes with respect to the OGVs and turbine are shown in Fig. 2. The figure also shows the location of the static pressure taps on the OGV.

In order to position the aero-probes, the TRS test section is instrumented with two cylindrical independent traversing systems that are capable of moving in the radial and circumferential directions. Moreover, the downstream probe can be traversed in the axial direction and therefore, the full volume of the TRS can be covered. The accuracy in the positioning of aero probes is 0.01 deg in a circumferential direction and 0.075 mm in axial and radial directions.

To measure the static pressure distributions a midvane of each measurement sector was manufactured with SLA rapid prototyping technology. The vane surface was equipped with 0.7-mm diameter pressure taps located along four spans. Three of the spans (25, 50, and 75%) were used for measurements of pressure distribution over the lower and upper surface of the OGV while a fourth span (12.5%), closest to the hub, was used to obtain static pressure values only on the OGVs suction side. In addition, for the bump vane, the bump was equipped with 96 pressure taps covering the entire bump surface.

A 16-channel digital pressure scanner (PSI-9116, Pressure Systems, Inc., Phoenix, AZ) with a 500-Hz sampling rate was used to acquire pressure values. The sampling time was 2.5 s. Twelve of the unit's channels were connected to the aero probes while two channels were dedicated to Scanivalve pressure multiplexers for wall static pressure measurements. The remaining two channels were used to obtain reference pressure values from the pitot-static tube located in the bulk region downstream of the OGVs. The static and total pressure data were converted to nondimensional pressure coefficients (Eqs. (1) and (2)) using reference pressures

$$C_{p0} = \frac{P_{\mathrm{t}} - P_{\mathrm{tref}}}{P_{\mathrm{tref}} - P_{\mathrm{sref}}} \tag{1}$$

$$C_p = \frac{P_{\mathrm{s}} - P_{\mathrm{sref}}}{P_{\mathrm{tref}} - P_{\mathrm{sref}}} \tag{2}$$

Following a recent study by Jonsson [18], it was chosen to measure the relative pressure with respect to the total reference pressure taken from the pitot-static tube and normalize the values with the dynamic pressure from the pitot-static tube. This is done in order to increase the accuracy of the measurements. This conversion to the nondimensional form also helps to remove rig-related flow variations unavoidably present in the raw pressure data. Furthermore, other reference values were used for comparison with CFD. The total and static pressure reference values based on area averaging of inlet total and static pressure values were used and calculated as

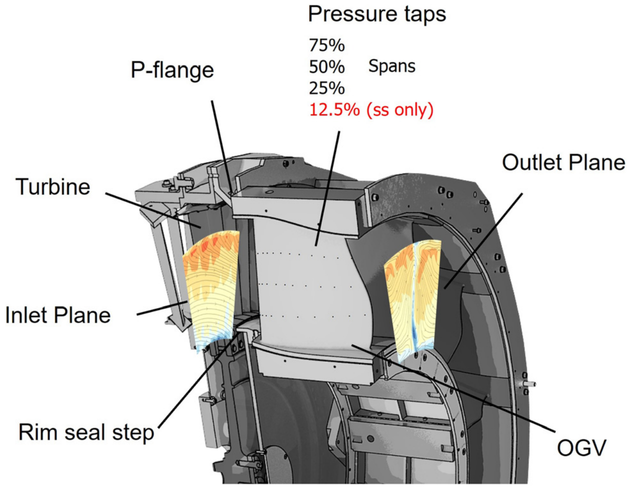

Fig. 2 Measurement planes and location of the static pressure taps on the OGV

Table 1 Operating conditions

	Operating conditions		
	Low loading/low swirl (sea-level takeoff)	On-design (cruise)	High loading/high swirl (climb point)
Inlet swirl angle	−6, 3	−16, 9	−22, 4
Flow coefficient	0.555	0.622	0.66
Reynolds number		350,000	

$$P_{\text{tref}} = \frac{\sum_i P_{\text{t,i}} A_{\text{i}}}{A} \quad P_{\text{sref}} = \frac{\sum_i P_{\text{s,i}} A_{\text{i}}}{A} \tag{3}$$

where A_{i} is the cell area around the ith node, A is the inlet plane area, and $P_{\text{t,i}}, P_{\text{s,i}}$ are total and static pressure values for the ith node.

The visualizations were performed by the oil-film method, which is a state-of-the-art tool for obtaining a qualitative survey of the near-surface flow. Based on previous experience, a mixture of oil and TiO_2 powder, with particles from 0.2 to 0.3 μm was selected. The flow patterns were captured by a digital camera whereafter surface streamlines were manually added to the images after dynamic analysis of the flow visualization sequences.

Regarding operating conditions, the experiments were carried out at three different flow coefficients, from 0.555 to 0.66. This corresponds to an average inlet swirl angle between 6.3 and −22.4 deg, thus spanning a range of 16.1 degrees. The on-design flow coefficient corresponds to the typical cruise flight conditions, the low-loading flow coefficient (low absolute swirl angle) corresponds to sea-level takeoff conditions, and the high-loading flow coefficient (high absolute swirl angle) corresponds to a climb point, all points where performance is important. With the Reynolds number set to 3.5×10^5 the inlet flow characteristics are representative of a TRS in a narrow body geared turbofan engine. The TRS operating conditions including the on-design point are summarized and presented in Table 1.

3 Numerical Setup

The numerical simulations are done using the commercial CFD solver FLUENT 2019R3 by ANSYS. The regular, thick and bump vane are simulated one at a time in a sectorized, single vane model. The computational domain of each sector is meshed by hexahedral elements in the commercial mesh tool ICEM 2019R1. The near-wall grid is resolved to achieve $y+$ values below unity in all cases. The computational domains consist of an average of 2.3 M cells, and the final mesh resolution is based on the results from previous mesh sensitivity study. Rotational periodic interfaces are applied on the circumferential boundaries. The circumferential extent of the computational domain in each sector is 30 deg. The computational domain with the mesh resolution on the wall boundaries of the regular vane sector is shown in Fig. 3.

Steady-state RANS simulations are done using the four-equation transition-SST turbulence model by Langtry-Menter [19], also known as the gamma Retheta (γ−Re_θ) model. This turbulence model solves for the k–ω transport equations and adds two other transport equations, one for the intermittency (γ) and one for the transition onset criteria in terms of the momentum thickness Reynolds number (Re_θ). The model constants in the turbulent transport equations are kept at default in the simulations.

Total pressure and flow angle measurements from the five-hole probe on the inlet plane (Fig. 2) are used to compute the inlet boundary conditions for the numerical analyses in each sector at each flow condition. The measurements' data are used to compute circumferentially averaged radial profiles of total pressure and

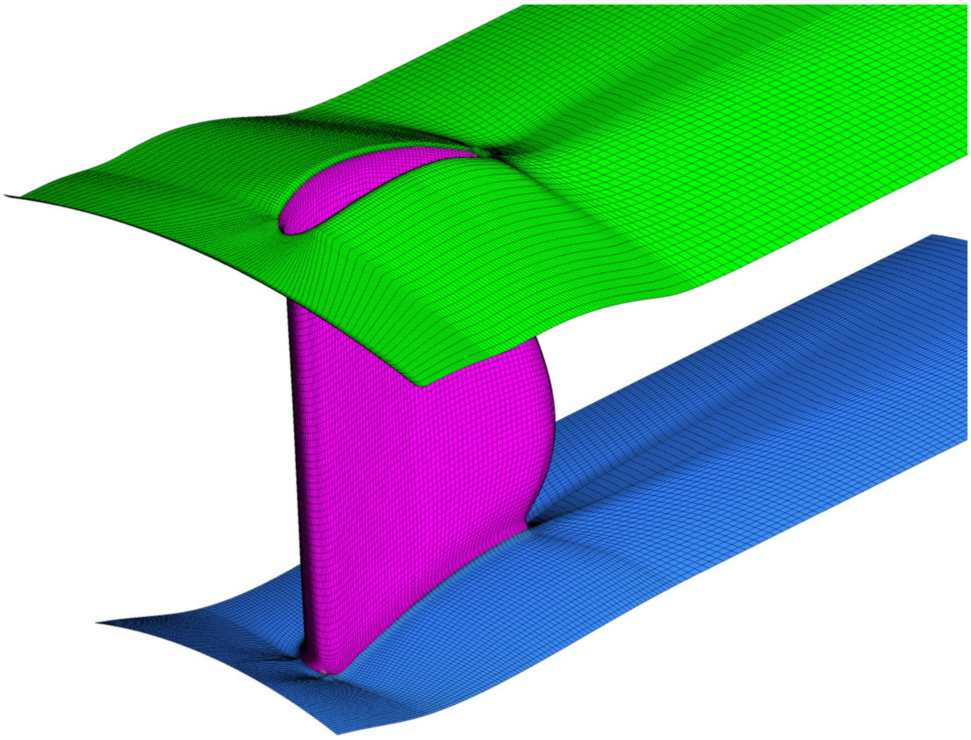

Fig. 3 The computational domain of the regular sector with wall resolution on hub, vane, and shroud

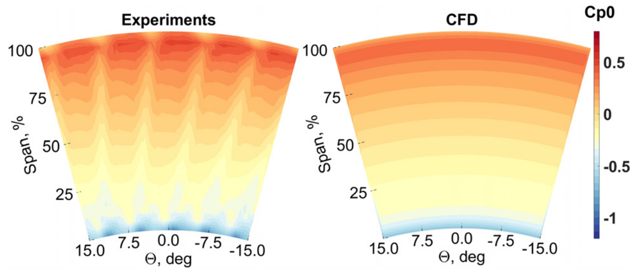

Fig. 4 Typical inlet total pressure contours (for thick vane at FC = 0.555)

flow angle components. The radial profiles are applied at the inlet of the computational domain. Inlet turbulence conditions are kept the same and constant in all simulations.

An average static pressure is set as outlet boundary condition. A radial equilibrium static pressure boundary is used on the outlet, where the static pressure is adjusted to obtain the same mass flow as measured in the experiments. All walls are treated as adiabatic and with smooth no-slip condition.

Surface streamlines in Sec. 4.3 are generated in CFD-Post 2019R3. Other numerical data are visualized using MathWorks MATLAB.

4 Results and Discussion

In this section, wall static pressure, total pressure, and swirl angle distributions, as well as flow visualizations, are presented. The results are used to analyze the flow in the TRS and to validate the CFD simulations. The performance of the TRS is considered from the aerodynamic point of view. The performance of CFD is evaluated for prediction capabilities of the TRS aerodynamic performance and secondary flows.

4.1 Inlet Conditions. Inlet measurements of total pressure and flow angles were made for a 30-deg sector located upstream of the OGV. Figure 4 shows typical inlet total pressure contours obtained experimentally, and the corresponding inlet values used in CFD. Circumferentially averaged values were used in CFD, which means that the circumferential flow nonuniformities were not modeled in the numerical simulations.

The contour plot from the experiment clearly shows five stator wakes coming from upstream NGVs. The wakes are evidenced by the reduced total pressure coefficient. Moreover, counter-rotating vortex pairs coming from each NGV in the hub and shroud regions are clearly visible. The total pressure increases from hub to shroud as expected (Fig. 5 and Ref. [13]) and the absolute value of the inlet swirl decreases (Fig. 5). Experimental profiles are obtained at the on- and off-design conditions (see Table 1).

The largest inlet swirl magnitude is near the hub, decreasing toward zero near the shroud and attaining opposite swirl direction in the leakage flow region near the shroud. The swirl magnitude increases with the flow coefficient as expected. Notably, the bump vane is showing clear upstream influence on the swirl distributions near the hub and shroud. Furthermore, the bump vane has a pronounced upstream influence on the entire inlet total pressure profile. The thick vane has some visible upstream effect on total pressure near the hub wall and not influencing the inlet swirl. For all cases, the radial gradient of the total pressure is decreasing with increased flow coefficient as shown earlier [13,14]. The inlet profiles illustrate as well that the flow near the shroud is affected by the leakage via the turbine seal and by the presence of the upstream P-flange pocket, shown in Fig. 2. The flow near the hub is disturbed by the rim seal step positioned between the stationary and rotating parts.

4.2 Vane Static Pressure Distributions. This section presents vane static pressure distributions, comparing CFD simulations and experiments at 50% span. Measurements are made on all vane types, at the on-design inlet swirl condition (FC = 0.622), at the low-swirl off-design condition (FC = 0.555) and at the high-swirl off-design condition (FC = 0.66).

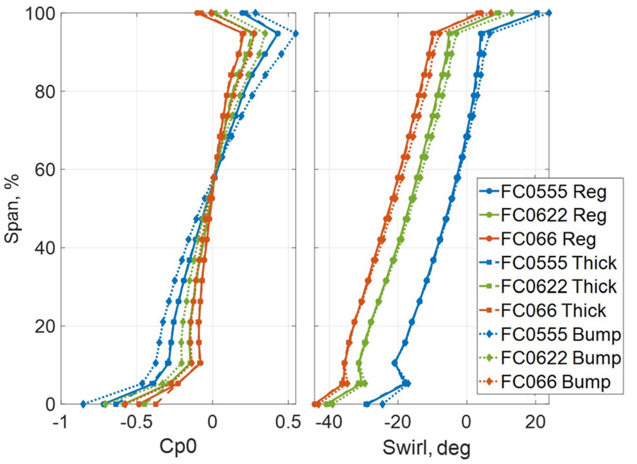

Fig. 5 Circumferentially averaged inlet total pressure coefficient (left) and swirl angle (right) for the regular, thick, and bump vanes at on- and off-design flow coefficients

Figure 6 presents the vane static pressure distributions from the measurements and numerical analyses of all vanes and all flow conditions. Measurement results are shown as symbols and CFD results with solid lines.

The numerical predictions agree very well with the measurements. At the design condition (FC = 0.622) all three vane types show similar pressure distributions, with well-placed pressure peaks and no large over-accelerations around the leading edges. As desired, there is a reduced deceleration close to the trailing edges, where the boundary layers are sensitive to flow separation.

At the reduced swirl off-design condition (FC = 0.555) all three vane types show a local pressure side over-acceleration around the leading edge. However, the following diffusion is acceptable and no large pressure side separations can be seen. On the suction side, the suction peaks are, as expected, reduced and moved aft. Hence, all three vane types show robust aerodynamics and do not show any separation tendencies at the low-swirl off-design condition (FC = 0.555).

At the increased swirl condition (FC = 0.66), the suction peaks are, as expected, increased in magnitude and moved forward for all vane types. The pressure distributions are still well-conditioned and there is no local over-acceleration or additional small suction peaks at the leading edges. The loading and the deceleration close to the trailing edges still appear well controlled without any signs of separation. All three vane types show robust behavior also at this high swirl condition.

Looking closely at the measurements and comparing them with the numerical results one can see stronger diffusion on the suction sides just downstream of the suction peaks. As was shown in a thorough analysis of Jonsson et al. [12], and supported by the following flow visualizations, at increased inlet swirl, a laminar separation is triggered at midspan on vane suction side at $x/c = 0.4$. This flow separation is not captured by CFD since the CFD is predicting an earlier laminar-turbulent transition. However, since the laminar separation is rapidly reattached after the separation-induced transition, the influence of this separation on the downstream flow is minimal and not affecting the downstream losses in the midspan region.

4.3 Flow Visualizations. This section focuses on the analysis of characteristic flow features around OGVs and the influence of flow coefficient and shroud geometry on these features. A comparison between the experimental oil-film visualizations and the CFD

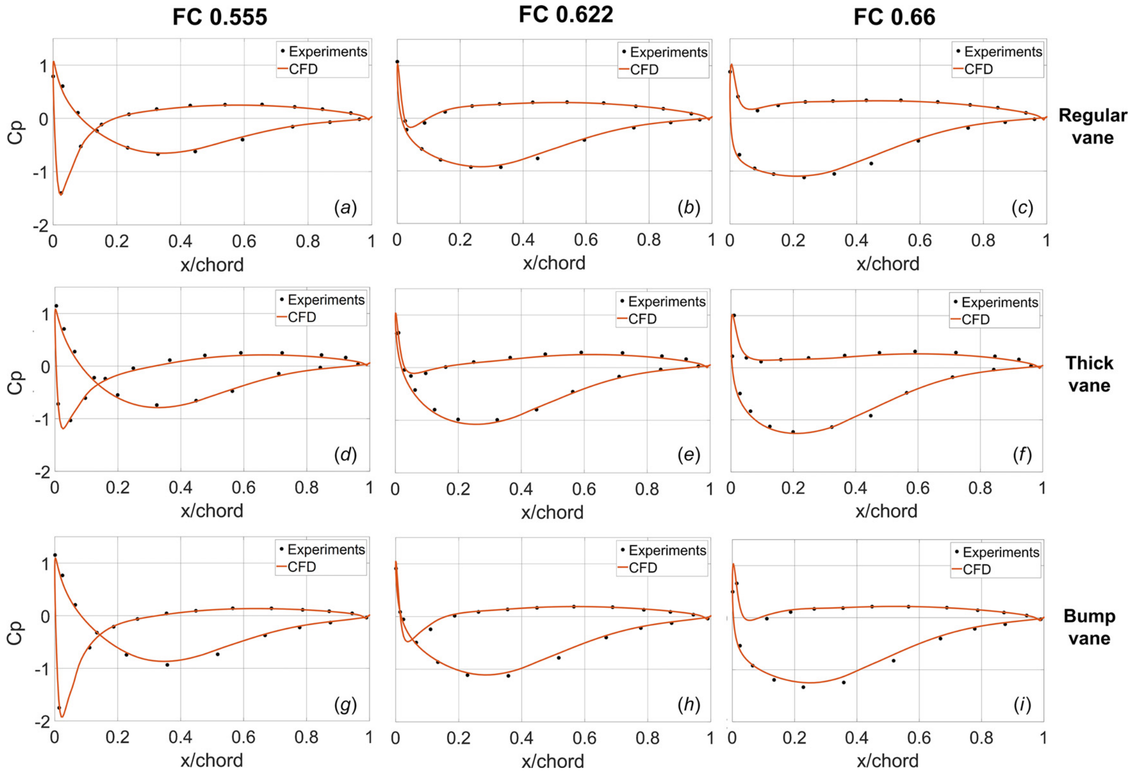

Fig. 6 CFD predictions and measurements of wall static pressure coefficient distributions at midspan of the regular, thick, and bump vanes at on- and off-design flow coefficients

predictions of near-wall streamlines is performed. Figures 7–10 present experimental and numerical flow visualizations on the thick and bump vanes at on-design and high loading off-design conditions.

These results are shown on the suction side of OGVs since hub suction side corner is found to be the most sensitive to flow separations and plays a significant role in pressure losses [13,14]. Detailed analysis of the flow processes that causes losses due to secondary flows was given by Sieverding et al. [20] and by Langston et al. [21].

The regular vane case is not shown for the reason that it is very similar to the thick vane case. The low loading case for the suction side is also omitted as it does not reveal any features of particular interest.

Figure 7 shows the flow visualizations for the thick vane at on-design condition. For the experimental case, two small regions with accumulated particles (marked with red solid lines) are clearly visible. The origin of these two regions can be explained by the presence of small local separation bubbles followed by further reattachment. A blue dashed line shows the expected location of laminar-turbulent transition based on the analysis for the previous configuration [11,12].

Note the position of this line at $x/c = 0.4$ at midspan; camera view angle and optical distortions make the location appear closer to the leading edge than the actual location.

For the previous configuration [12], a similar separation bubble formed at $x/c = 0.4$ and reattached on the laminar-turbulent transition line at $x/c = 0.5$. The CFD visualization does not indicate the laminar separation bubble at $x/c = 0.4$–0.5 observed in the experiment. Based on the previous findings [12], this is explained by the earlier laminar-turbulent transition in CFD. As a result, the turbulent boundary layer does not separate in CFD. It can be noted,

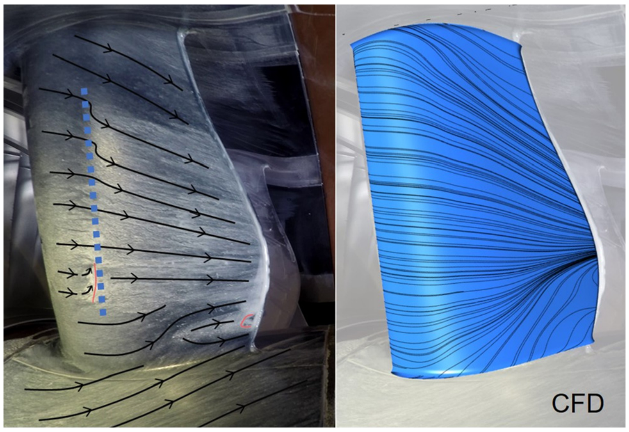

Fig. 7 Oil-film visualization (left) and near-wall streamlines from CFD (right) on a thick OGV suction side at on-design flow coefficient (FC = 0.622)

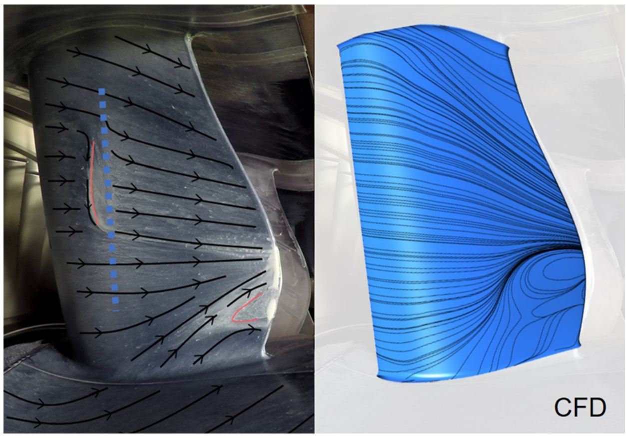

Fig. 8 Oil-film visualization (left) and near-wall streamlines from CFD (right) on a thick OGV suction side at off-design flow coefficient (FC = 0.66)

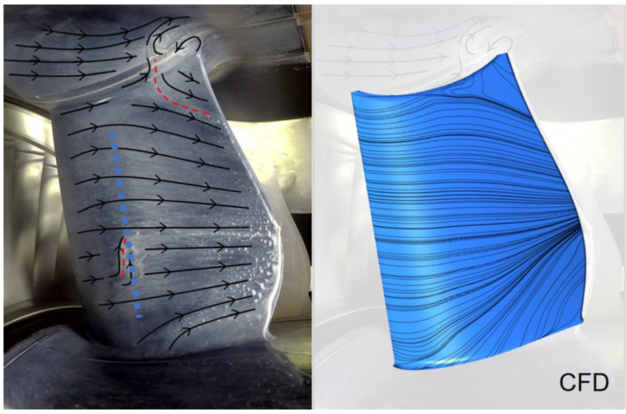

Fig. 9 Oil-film visualization (left) and near-wall streamlines from CFD (right) on a bump OGV suction side at on-design flow coefficient (FC = 0.622)

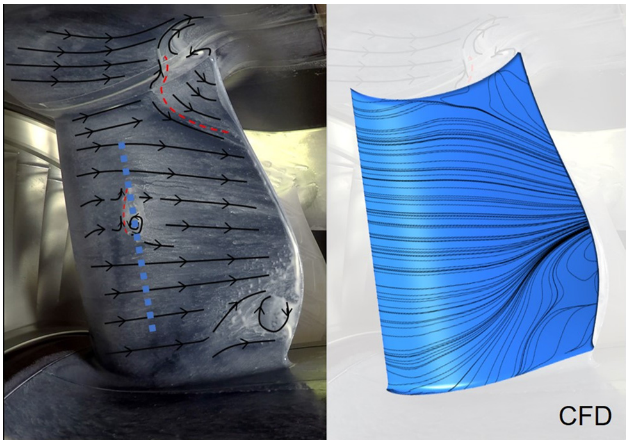

Fig. 10 Oil-film visualization (left) and near-wall streamlines from CFD (right) on a bump OGV suction side at off-design flow coefficient (FC = 0.66)

however, that this separation bubble with fast reattachment is not influencing downstream losses as discussed in the section Vane Static Pressure Distributions. One can observe a typical streamline deviation from hub and shroud toward the 1/3 of vane span in both experiment and CFD. As well, there is a typical streamline distortion near the shroud caused by a mixed effect of the radial pressure gradient and the polygonal shape of the shroud. In the hub corner region, the flow is strongly diffusive and three-dimensional.

For the increased vane loading (Fig. 8), the reverse flow region with accumulated particles near the leading edge is seen to grow and is shifted closer to the shroud, similarly to Ref. [13], while the diffusive hub corner region becomes larger and the separated zone in this region becomes larger.

The CFD simulations capture the increase of the corner region and the increase of the reverse flow zone; however, in CFD, the streamlines are more curved, and the reversal zone is larger. Additionally, the CFD result shows more profound flow deflection near the vane trailing edge in the shroud region, which can contribute to increased flow diffusion and pressure losses. As can be understood from the comparison of experiment and CFD, in the hub suction side corner close to the trailing edge, CFD overpredicts the size of the secondary flow region.

For the bump vane at on-design flow coefficient (Fig. 9), the experimental visualization shows flow separation upstream the transition line very similar to that of the thick vane. The flow in the hub corner region is similar to the thick vane as well. The shroud corner region is strongly affected by the bump and the CFD shows a very similar flow prediction near the vane trailing edge in the bump region. The streamline deflection in this region matches very well with the experiment.

The visualizations for increased loading case (Fig. 10) demonstrate clear changes in the surface streamlines. The small laminar separation bubble marked with a red dashed line is shifted toward the shroud as with the thick vane. Moreover, a region with reverse flow is created in the hub corner close to the vane trailing edge. CFD shows very good agreement with experimental results except the small laminar separation region upstream of the laminar-turbulent transition line similar to the thick vane case.

Figure 11 shows the flow visualizations on the pressure side of bump vane at FC = 0.555. It can be noted that there is a quasi-two-dimensional separation bubble formed along the leading edge on the pressure side at FC = 0.555 (marked with a red dashed line). The separation bubble extends about 5% chord in the streamwise direction and it is assumed that the flow reattachment occurs due to the laminar-turbulent transition. This separation bubble on the pressure side is not formed at FC = 0.622 or 0.66 and well captured with CFD for all vane cases. The flow streamlines on pressure side for other loading cases and other vanes are well predicted by CFD but not shown here.

4.4 Outlet Measurements.

In this section, a comparison is made of the outlet total pressure and swirl angle distributions for all nine cases.

Contours of normalized total pressure for the regular, thick and bump vanes at all three studied flow coefficients are presented in Fig. 12. Note that the wake data is shown for about half of the sector, showing the central part containing the OGV wakes. The figure shows a side-by-side comparison of experimental and numerical data. Note the reverse direction of the horizontal axes for agreement with physical setup in Fig. 1. The OGV wakes are shown from downstream the TRS module, while the polar angle increases to positive angles in direction of turbine rotation. In each contour plot the left part of the vane wake corresponds to the pressure side and the right part to the suction side.

For each vane type, one can observe that in experiments the wakes from the vanes are small at the on-design flow coefficient, FC = 0.622. In experiments, it can be noted that there is a relatively large region with reduced total pressure at FC = 0.555, which is located near the hub on the vane pressure side in all cases. The size of this region is visibly smaller in CFD, which is particularly pronounced for the bump vane case. It can be noted that the losses in this region are predicted rather well in CFD in terms of trends. CFD predicts the largest losses in this region for the bump vane at FC = 0.555 and for the other two vanes, this part

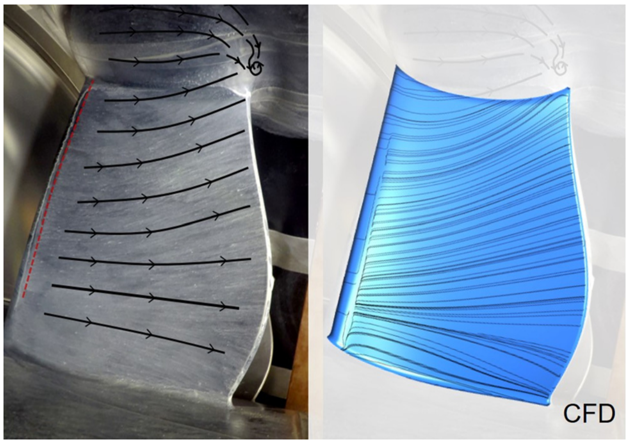

Fig. 11 Oil-film visualization (left) and near-wall streamlines from CFD (right) on a bump OGV pressure side at off-design flow coefficient (FC = 0.555)

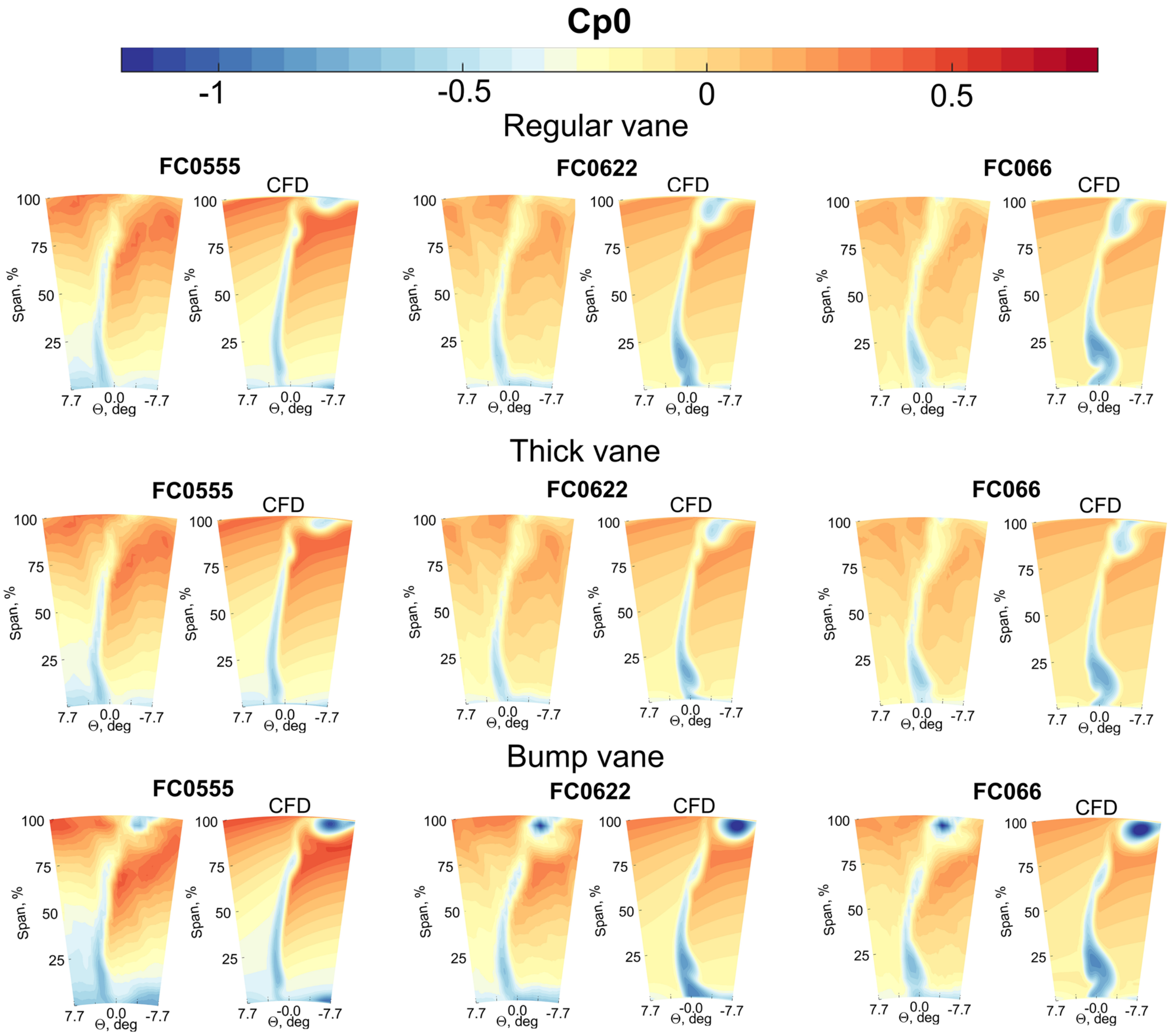

Fig. 12 Total pressure coefficient distributions at Outlet plane for regular, thick, and bump vanes at on- and off-design flow coefficients. In each contour plot: PS—to the left, SS—to the right.

has larger losses at FC = 0.555 as compared to other flow coefficients. Both these trends are captured very well by CFD.

Due to the inlet swirl-angle radial gradient (Fig. 5), the OGV load is larger in the lower spans close to the hub. This increases diffusion and secondary flows in the hub region. The hub boundary layer migrates toward the suction side and rolls up on the vane. A similar, although smaller, secondary flow loss region is formed near the shroud (Figs. 7–10).

Figure 12 shows these secondary flow loss regions close to the end walls in the suction side areas of the vane wakes. The secondary flows and the corresponding loss regions increase with increased absolute inlet swirl angle, i.e., larger flow coefficient, as expected. In CFD, this can be seen as a gradual increase of these loss regions as the absolute swirl angle and flow coefficient increases.

In experiments, however, there is no obvious change from FC = 0.555 to FC = 0.622, while there is a clear wake increase from FC = 0.622 to FC = 0.66. CFD overpredicts the secondary flows and the creation of the associated loss regions in the hub and shroud suction side corners. Overall, CFD predictions are conservative, which is favorable for a reliable design.

From the experimental flow visualization shown for the bump vane (Figs. 9 and 10), it is evident that apart from the notable flow redistribution, the boundary layers developed in the shroud region near the bump have separated both on the vane and on the bump itself. Hence, a strong vortical flow region with decelerated fluid is created. The analysis of the streamwise vorticity distributions in the wake, which is not provided here, though the experimental data were included in Ref. [14], shows that the vorticity magnitude in the core of this vortex is about twice as large as in the vane wake region. Therefore, this region with strong vorticity contributes to additional pressure losses, which are not present for the regular and thick vanes. The CFD simulations predict the increase of the pressure loss occurring in the bump region near the shroud with increased flow coefficient well, although the magnitude is overpredicted in CFD similar to other vane cases. For the current bump vane design, the bump itself shows acceptable aerodynamic performance. The current configuration has a dedicated mount vane, which results in an improved aerodynamic design of the vane-bump combination compared to the previous configuration [13]. The less optimized vane-bump design combination in the previous configuration resulted in additional substantial losses induced in the hub region, which is not observed for the current design.

Figure 13 presents detailed comparisons of total pressure wakes at different spans and flow coefficients for the thick vane.

Wake profiles are presented for a full angular range from 15 to −15 deg. As clearly seen, the wakes at midspan are predicted very

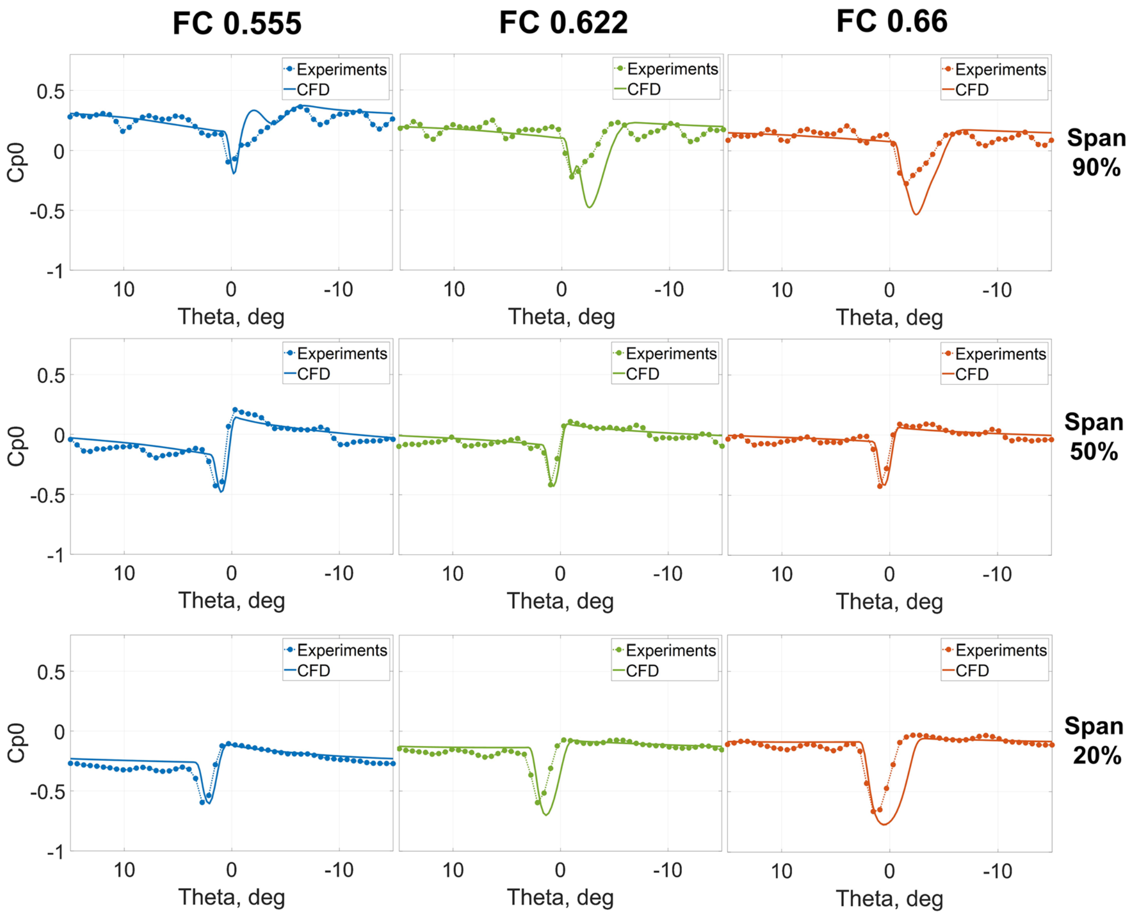

Fig. 13 Total pressure coefficient distributions for 90, 50, and 20% spans for the thick vane at on-design and off-design flow coefficients

well for all flow coefficients. In the midspan region, secondary flows are less important, and the simulations here predict losses and wake width very well. The wake widths and losses near the hub and shroud are about twice as large in CFD at FC = 0.622 and 0.66. This is caused by the previously described over-prediction of secondary flows in these cases.

For the reduced load case (FC = 0.555), there is some underprediction of the wake near the shroud and some underprediction outside of the wake on the pressure side (PS) region with $\theta = 2$–15 deg. The relative change of the wakes with the flow coefficient can clearly be evaluated. The flow becomes more diffusive in the hub region for increased flow coefficient and this translates to the enlargement of the wake width, as discussed above.

Figure 14 presents comparisons of circumferentially averaged downstream total pressure coefficient for the same cases as in Fig. 12. It can be noticed that the averaged CFD profiles are generally in good agreement with experiments. However, in the regions with intensive secondary flows close to the end walls, the CFD predictions show some differences from the experiments. In the shroud region, at 70–100% span, some differences can be observed for all nine cases. This is the region where the polygonal shroud and circular-polygonal transition regions are located. For the regular and thick vanes at flow coefficient 0.555, CFD overpredicts the losses near the shroud at 85–95% span and underpredicts in close proximity to the shroud. The explanation for this can be seen in the total pressure contours (Fig. 12), where CFD results overpredict the secondary flow structures. The differences are larger for the bump vane case at FC = 0.555 and overall overprediction can be observed. In the hub region, there is also a typical overprediction of the variations related to the secondary flow structures for all nine cases. For all three vane geometries, the shape of the total-pressure profiles is very similar and the difference between the CFD and experiments in the strong secondary flow regions near the hub and shroud is relatively small at the on-design flow coefficient, FC = 0.622. The total pressure profiles in the region away from the end walls show the smallest difference between measurements and CFD predictions.

The goal of the aero designer is to design a TRS that deswirls the flow from the LPT by introducing minimal additional pressure losses, thus obeying two key design criteria.

The performance of the current OGVs regarding deswirling the flow from the LPT to axial flow is illustrated in Fig. 15. The figure shows the circumferentially averaged downstream profiles of outlet swirl angle for all studied cases. The aim of a good design is to have the outlet swirl angles close to zero. For the regular and thick vane, the following trends can be seen. In the vicinity to the end walls, CFD predicts the flow turning well. In the bulk flow at 40–80% span, CFD predicts overturning of the flow with approximately 1 degree relative to the experiments. At 10% span, CFD predicts under-turning of the flow with approximately 1 degree in reference to the experiments. The explanation to this is overprediction of secondary flow structures in the CFD simulations as discussed before. For the bump vane, the flow angle profiles demonstrate a very characteristic swirl change in the shroud region. CFD simulation predicts very well the location of the swirl change and the flow turning in this region, which is a very encouraging result. The best overall prediction is observed for the bump vane at FC = 0.555 and for all other cases the prediction of turning is very satisfactory. It is particularly notable that the outlet swirl is closest to zero at on-design flow coefficient (FC = 0.622), as intended. The CFD predictions follow the profile variation with

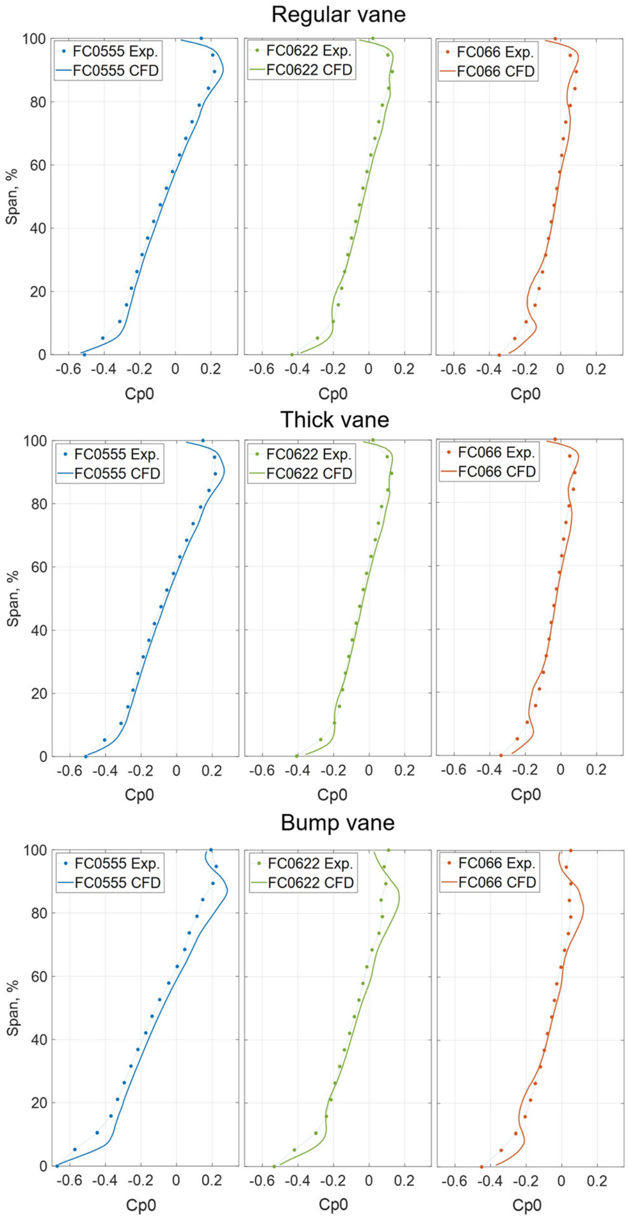

Fig. 14 Circumferentially averaged total pressure coefficient for the regular, thick and bump vanes at on- and off-design flow coefficients

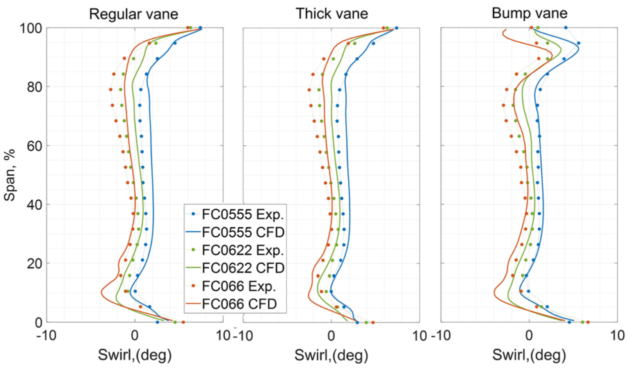

Fig. 15 Circumferentially averaged outlet swirl angle for the regular, thick and bump vanes at on- and off-design flow coefficients

varied flow coefficient well, where the residual swirl increases with increased flow coefficient. A good prediction of the flow turning angle from the TRS is very important since an incorrect flow turning will result in additional losses due to the residual swirl present in the aero-engine wake.

Figure 16 shows experimental and numerical Zweifel coefficients for all studied cases. As clearly seen, Zweifel coefficient increases with increased flow coefficient. Regular and thick vanes show similar loading, which can be explained that overall aerodynamic performance between two vanes is similar. For the bump vane, Zweifel coefficient is lower due to the presence of shroud bump and, hence, reduced inlet swirl angle. However, on-design Zweifel coefficients are optimal and meet general design requirements ($Zw \sim 0.7$–0.8). It can be noted that CFD predicts the Zweifel coefficient well with accuracy better than 0.02 counts for all cases.

5 Summary and Conclusions

Aerodynamic measurements and numerical analysis of an engine realistic state-of-the-art TRS with polygonal outer case, recessed engine mount bumps, and three different vane types were performed. The study was undertaken in an environment relevant for a geared turbofan engine at Reynolds number of 350,000 at three different inlet swirl conditions. The numerical results demonstrate good agreement with experiments.

The thick vane shows aerodynamic performance very similar to the regular vane. There is an increase in vane loading with the presence of the mount bump, causing deeper suction peaks on both suction side (SS) and PS compared to the regular and thick vanes. CFD simulations accurately predict the axial location and depth of suction peaks and diffusion rate aft of the suction peaks on all vanes at all flow conditions.

The comparison of circumferentially averaged radial outlet total pressure profiles shows good agreement outside of the near endwall regions. CFD predicts larger loss variations in the vicinity of the hub and shroud compared to measurements. The increased loss variations are due to overprediction of secondary flow structures in CFD. These structures were visualized using the oil-film method in measurements and surface streamlines in CFD and shown to affect the wake width near the hub and shroud regions. CFD overpredicts these wake regions compared to measurements, and the difference increases with increased flow coefficients. Wakes at less loaded flow coefficients, and in the midspan region where the secondary flow structures are less pronounced, are well predicted by CFD.

Moreover, a strong vorticity region evidenced with local pressure drop near the shroud is seen in the bump vane wake. The loss vortex is a consequence of both bump design and acting pressure gradient. This loss vortex is also predicted by CFD, but with somewhat larger extent and magnitude.

From the circumferentially averaged outlet swirl profiles, CFD predictions show good agreement with the measurements. CFD predicts under-turning in highly loaded sections, which is a consequence of the overprediction of secondary flow structures and hence prediction of earlier flow separation as compared to the measurements. In less loaded regions, where the flow is less prone to separation, CFD predicts overturning of the flow. The measured and predicted loss vortex in the bump sector affects the outlet residual swirl, which is well captured by CFD.

The visualizations at $\mathrm{FC} = 0.622$ and 0.66 indicate laminar separation bubbles at $x/c = 0.4$–0.5, which is not captured by CFD. According to the previous thorough analysis [12], this is a result of earlier prediction of the laminar-turbulent transition by the $\gamma - \mathrm{Re}_\theta$ model. However, since the laminar separation is rapidly reattached after the separation-induced transition, this separation is not affecting the downstream losses in the midspan region. At $\mathrm{FC} = 0.555$, there is a quasi-two-dimensional separation bubble formed along the leading edge on the pressure side. This

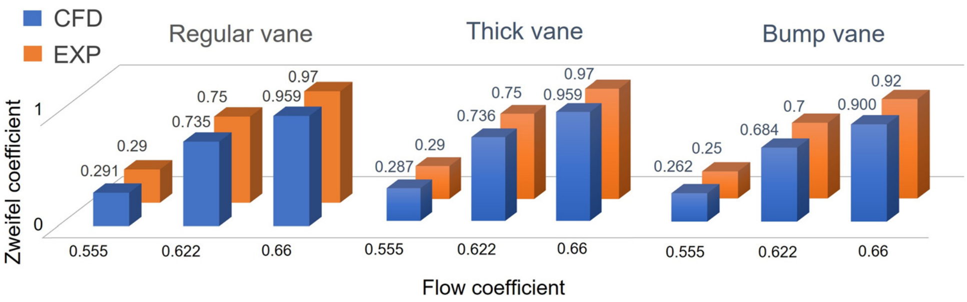

Fig. 16 Experimental and numerical Zweifel coefficients for the regular, thick and bump vanes at on- and off-design flow coefficients

separation bubble is not formed at other inlet swirl cases and well captured with CFD for all three vane types.

The engine realistic TRS with all three vane types mounted simultaneously showed a different upstream influence of different vane types on inlet boundary conditions, which is crucial for accurate modeling of TRS aerodynamics

Acknowledgment

The authors would like to gratefully acknowledge financial support from the NFFP (Nationella flygtekniska forskningsprogrammet) and the EU Commission. This project has received funding from the Clean Sky 2 Joint Undertaking under the European Union's Horizon 2020 Research and Innovation Program under Grant Agreement No. 821398. Chalmers Laboratory of Fluids and Thermal Sciences is acknowledged for hosting the facility and the measurement equipment.

Funding Data

- Vinnova (Funder ID: 10.13039/501100001858).
- Clean Sky 2 Joint Undertaking under the European Union's Horizon 2020 Research and Innovation Program (Grant Agreement No. 821398; Funder ID: 10.13039/501100000922).

Nomenclature

C_p = static pressure coefficient, $(P_s - P_{sref})/(P_{tref} - P_{sref})$
C_{p0} = total pressure coefficient, $(P_t - P_{tref})/(P_{tref} - P_{sref})$
FC = flow coefficient
H = channel height at inlet, m
LE = leading edge
LPT = low pressure turbine
NGV = nozzle guide vane
OGV = outlet guide vane
P_s = static pressure, Pa
P_t = total pressure, Pa
PS = pressure side
Re = Reynolds number, $U_x H/\nu$
SS = suction side
TRS = turbine rear structure
U_x = axial flow velocity, m/s
V = blade velocity, m/s
x = streamwise coordinate, m
Zw = Zweifel coefficient
θ = angular coordinate, deg
ν = kinematic viscosity, m^2/s
φ = flow coefficient, U_x/V

References

[1] Hjärne, J., Larsson, J., and Löfdahl, L., 2006, "Performance and Off-Design Characteristics for Low Pressure Turbine Outlet Guide Vanes: Measurements and Calculations," ASME Paper No. GT2006-90550.

[2] Hjärne, J., Larsson, J., and Löfdahl, L., 2003, "Design of a Modern Test Facility for LPT/OGV Flows," ASME Paper No. GT2003-38083.

[3] Hjärne, J., Chernoray, V., Larsson, J., and Löfdahl, L., 2005, "Experimental Evaluation of the Flow Field in a State-of-the-Art Linear Cascade With Boundary Layer Suction," ASME Paper No. GT2005-68399.

[4] Hjärne, J., Chernoray, V., Larsson, J., and Löfdahl, L., 2006, "An Experimental Investigation of Secondary Flows and Loss Development Downstream of a Highly Loaded Low Pressure Turbine Outlet Guide Vane Cascade," ASME Paper No. GT2006-90561.

[5] Hjärne, J., Chernoray, V., and Larsson, J., 2008, "Experimental Investigations and Numerical Validation of an Outlet Guide Vane With an Engine Mount Recess," ASME Paper No. GT2008-50168.

[6] Hjärne, J., Chernoray, V., Larsson, J., and Löfdahl, L., 2007, "Numerical Validations of Secondary Flows and Loss Development Downstream of a Highly Loaded Low Pressure Turbine Outlet Guide Vane Cascade," ASME Paper No. GT2007-27712.

[7] Rojo, B., Kristmundsson, D., Chernoray, V., Arroyo, C., and Larsson, J., 2015, "Facility for Investigating the Flow in a Low Pressure Turbine Exit Structure," Proceedings of 11th European Conference on Turbomachinery Fluid Dynamics and Thermodynamics, ETC 2015, Spain, Madrid, Mar. 23–25, Paper No. ETC2015-235.

[8] Rojo, B., 2017, "Aerothermal Experimental Investigation of LPT-OGVs," Ph.D. thesis, Chalmers University of Technology, Gothenburg, Sweden.

[9] Jonsson, I., Chernoray, V., and Rojo, B., 2018, "Surface Roughness Impact on Secondary Flow and Losses in a Turbine Exhaust Casing," ASME Paper No. GT2018- 75541.

[10] Jonsson, I., Chernoray, V., and Dhanasegaran, R., 2019, "Infrared Thermography Investigation of Heat Transfer on Outlet Guide Vanes in an Engine Exit Module," Proceedings of 13th European Turbomachinery Conference on Turbomachinery Fluid Dynamics and Thermodynamics, ETC 2019, Switzerland, Lausanne, Apr. 7–11, Paper No. ETC2019-243.

[11] Deshpande, S., Jonsson, I., and Chernoray, V., 2019, "Effect of Surface Roughness on Aerodynamic Performance of Turbine Rear Structure," ASME Paper No. GT2019-90472.

[12] Jonsson, I., Deshpande, S., Chernoray, V., Thulin, O., and Larsson, J., 2020, "Experimental and Numerical Study of Laminar-Turbulent Transition on a Low-Pressure Turbine Outlet Guide Vane," ASME Paper No. GT2020-1787.

[13] Vikhorev, V., Chernoray, V., Thulin, O., Srikanth, D., and Larsson, J., 2020, "Detailed Experimental Study of the Flow in a Turbine Rear Structure at Engine Realistic Flow Conditions," ASME Paper No. GT2020-15734.

[14] Vikhorev, V., and Chernoray, V., 2021, "Experimental Flow Analysis in a Modern Turbine Rear Structure With 3D Polygonal Shroud Under Realistic Flow Conditions," Proceedings of 14th European Turbomachinery Conference on Turbomachinery Fluid Dynamics and Thermodynamics, ETC 2021, Gdansk (Virtual), Poland, Apr. 12–16, Paper No. ETC2021-539.

[15] Selic, T., Lengani, D., Marn, A., and Heitmeir, F., 2012, "Aerodynamic Effects of an Unshrouded Low Pressure Turbine on a Low Aspect Ratio Exit Guide Vane," ASME Paper No. GT2012-68981.

[16] Simonassi, L., Zenz, M., Zerobin, S., Selic, T., Heitmeir, F., and Marn, A., 2019, "On the Influence of an Acoustically Optimized Turbine Exit Casing Onto the Unsteady Flow Field Downstream of a Low Pressure Turbine Rotor," ASME J. Turbomach., **141**(4), p. 041003.

[17] Zenz, M., Asim, H., Simonassi, L., Leitl, P., Benauer, R., Heitmeir, F., and Marn, A., 2019, "Aerodynamical and Aeroelastic Investigations of a Riblet Design Applied on the Surface of Turbine Exit Guide Vanes of a Low Pressure Turbine," Proceedings of 14th European Turbomachinery Conference, ETC 2019, Switzerland, Lausanne, Apr. 7–11, Paper No. ETC2019-055.

[18] Jonsson, I., 2020, "Experimental Aerothermal Study on Internal Jet Engine Structures," Licentiate thesis, Chalmers University of Technology, Gothenburg, Sweden.

[19] Menter, F. R., Langtry, R. B., Likki, S. R., Suzen, Y. B., Huang, P. G., and Völker, S., 2006, "A Correlation-Based Transition Model Using Local Variables—Part I: Model Formulation," ASME J. Turbomach., **128**(3), pp. 413–422.

[20] Sieverding, C. H., 1985, "Recent Progress in the Understanding of Basic Aspects of Secondary Flows in Turbine Blade Passages," ASME J. Eng. Gas Turbines Power, **107**(2), pp. 248–257.

[21] Langston, L. S., Nice, M. L., and Hooper, R. M., 1977, "Three Dimensional Flow in a Turbine Cascade Passage," ASME J. Eng. Gas Turbines Power, **99**(1), pp. 21–28.